Editors' Suggestion | Featured in Physics

Relating Rheotaxis and Hydrodynamic Actuation using Asymmetric Gold-Platinum Phoretic Rods

Quentin Brosseau,[1] Florencio Balboa Usabiaga,[2] Enkeleida Lushi,[3] Yang Wu,[4] Leif Ristroph,[1] Jun Zhang,[1,5,6] Michael Ward,[4] and Michael J. Shelley[1,2]

[1]*Courant Institute, New York University, New York, New York 10012, USA*
[2]*Center for Computational Biology, Flatiron Institute, New York, New York 10010, USA*
[3]*Department of Mathematics, New Jersey Institute of Technology, Newark, New Jersey 07102, USA*
[4]*Department of Chemistry, New York University, New York, New York 10012, USA*
[5]*Department of Physics, New York University, New York, New York 10003, USA*
[6]*New York University-East China Normal University Institute of Physics, New York University Shanghai, Shanghai 200062, China*

(Received 13 June 2019; revised manuscript received 20 August 2019; published 25 October 2019)

We explore the behavior of micron-scale autophoretic Janus (Au/Pt) rods, having various Au/Pt length ratios, swimming near a wall in an imposed background flow. We find that their ability to robustly orient and move upstream, i.e., to rheotax, depends strongly on the Au/Pt ratio, which is easily tunable in synthesis. Numerical simulations of swimming rods actuated by a surface slip show a similar rheotactic tunability when varying the location of the surface slip versus surface drag. The slip location determines whether swimmers are pushers (rear actuated), pullers (front actuated), or in between. Our simulations and modeling show that pullers rheotax most robustly due to their larger tilt angle to the wall, which makes them responsive to flow gradients. Thus, rheotactic response infers the nature of difficult to measure flow fields of an active particle, establishes its dependence on swimmer type, and shows how Janus rods can be tuned for flow responsiveness.

DOI: 10.1103/PhysRevLett.123.178004

Swimming microorganisms must contend with boundaries and obstacles in their natural environments [1–3]. Microbial habitats have ample surfaces, and swimmer concentrations near them promote attachment and biofilms 4,5]]. Motile bacteria and spermatozoa accumulate near boundaries, move along them [6,7], and self-organize under confinement [8–11]. Microswimmers also exhibit *rheotaxis*, i.e., the ability to actively reorient and swim against an imposed flow [12]. Surfaces are key for rheotactic response: fluid shear near boundaries results in hydrodynamic interactions which favor swimmer alignment against the oncoming flow and prevent swimmer displacements across streamlines [13–17]. Swimmers with different propulsion mechanisms—front actuated like puller microalgae or rear actuated like pusher bacteria—exhibit associated dipolar flow fields [18–20] which result in dissimilar collective motions [21–23] and behavior near boundaries or in flows [24–29].

Recent advances in the manufacture and design of artificial swimmers have triggered an acute interest in developing synthetic mimetic systems [3,30–34]. Like their biological counterparts, artificial swimmers can accumulate near boundaries [35,36], navigate along them [37,38], be guided by geometric or chemical patterns [39–42] or external forces [43,44], and can display rheotaxis near planar surfaces [45–47]. While models have been developed to study their locomotion and behavior [24,35,48,49], the relevance of the swimmers' actuation mechanism and the resulting hydrodynamic contributions to their rheotactic motion remains an open question. In large part this is due to the difficulty in directly assessing swimmers' flow fields, particularly near walls, and relating experimental observations to our theoretical understanding of swimmer geometry, hydrodynamics, and type (i.e., pusher or puller).

In this Letter, we address this question with experiments using chemically powered gold-platinum (Au/Pt) microswimmers combined and compared with numerical simulations. In experiments we vary the position of the Au/Pt interface along the swimmer length, postulating that this varies the location of the flow actuation region, and that observed differences in rheotaxis can be related to having different pusherlike or pullerlike swimmers. In simulation, we study the rheotactic responses of rodlike microswimmers that move through an active surface slip. Different placements of the slip region allow us to create pullers, symmetric, and pusher microswimmers. We find measurably different rheotactic responses in simulation which show quantitative agreement with our experiments with Au/Pt active particles conducted in microfluidic channels.

Experimental setup and measurements.—Our Janus microswimmers are elongated Au/Pt rods, $\sim 2\ \mu$m in length and $d \sim 0.3\ \mu$m in diameter, which propel themselves through self-electrophoresis in aqueous H_2O_2 solutions [32,34]. The swimmers are synthesized by

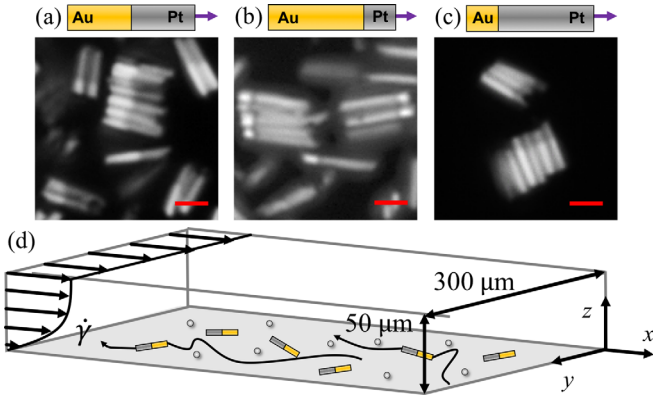

FIG. 1. Micrographs of the different bimetallic swimmers obtained with reflection microscopy (wavelength 495 nm). The ratio of the metallic segments varies from (a) 1:1 for symmetric, to (b) 3:1 for long gold, and to (c) 1:3 for short gold. Scale bar 1 μm. (d) Each swimmer type is tested in a rectangular microfluidic channel where it is gravitationally confined near the bottom. Under shear flow the metallic particles swim upstream.

electrodeposition [30,50] to a prescribed ratio of the two metallic segments: symmetric with Au:Pt (1:1), asymmetric long gold with Au:Pt (3:1), and asymmetric short gold with Au:Pt (1:3); see Figs. 1(a)–1(c) and details in Ref. [51].

The swimmers' rheotactic abilities are tested in a rectangular polydimethylsiloxane microfluidic channel of width $W = 300$ μm built following classical soft-lithography techniques [52]. We control the background unidirectional flow down the channel (the x direction) using an off-stage hydrostatic column. Suspended glass beads of radius $r_b \sim 2.5$ μm serve as markers to measure the flow profile close to the bottom of the channel where the rods move. We record the trajectories of swimmers and beads over 1 min and extract the instantaneous velocities of swimmers V_x and of beads U_b, along the x axis. See Fig. 1(d) and videos in Ref. [51].

Thermal fluctuations are important at this scale and the swimmers' means square displacement in quiescent fluid are used to estimate their translational and rotational diffusivities, D_t and D_r, and deterministic baseline swimming speeds V_0 [31,51]. At fixed H_2O_2 concentration, swimming speeds are smaller for asymmetric rods than for symmetric ones; therefore H_2O_2 concentration is adjusted to maintain a comparable velocity V_0 between experiments.

The background flow profile close to the wall $U_0(z)$ is measured by the drift velocity U_b of the suspended glass beads. As the beads move close to the wall, we find it important to account for the lubrication forces that act upon them [53]. The flow velocity is estimated to be $U_0(r_b + h_{\mathrm{th}}) \sim 2.5U_b$ for a thermal height $h_{\mathrm{th}} \sim 4$ nm [51].

Model and simulations.—Resolving the chemical and electrohydrodynamics near a wall is challenging. The electro-osmotic flow near a self-diffusiophoretic swimmer is the result of charge gradients localized on a small surface region near the junction of the two metallic segments [30]. We make the simplifying assumption that this results in a surface slip velocity yielding the rod propulsion with the Pt segment leading. As we do not know the extent of the slip region, we simply assume that it covers half the rod length. The propulsion speed depends on the slip coverage.

We model the swimmer as a rigid, axisymmetric rod immersed in a Stokes flow and sedimented near an infinite substrate. The rod is discretized using N_b "blobs" at positions $(\boldsymbol{r}_i - \boldsymbol{q})$ with respect to the rod center $\boldsymbol{q}$ [51,54,55]. Linear and angular velocities $\boldsymbol{u}$ and $\boldsymbol{\omega}$ satisfy the linear system Eqs. (1) and (2) where $\boldsymbol{\lambda}_i$ are unknown constraint forces enforcing rigid body motion and $\boldsymbol{M}$ is a regularization of the Green's function of the Stokes equation that accounts for the hydrodynamic interactions between blobs. Here we use the Rotne-Prager mobility tensor [56] corrected to include the hydrodynamic effect of the substrate [57,58].

Equation (1) represents the balance of the geometric constraint forces with the external force $\boldsymbol{F}$ and torque $\boldsymbol{\tau}$ generated by steric interactions with the substrate and gravity [51]. Equation (2) gives the balance of fluid, propulsive, and thermal forces, with $\tilde{\boldsymbol{u}}_i$ the active slip velocity, $\boldsymbol{u}_0(\boldsymbol{r}_i)$ the background flow velocity, and $\sqrt{2k_BT/\Delta t}(\boldsymbol{M}^{1/2}\boldsymbol{W})_i$ the Brownian noise, with k_B the Boltzmann constant, T the temperature, Δt the time step, $\boldsymbol{W}$ a vector of white noises, and $\boldsymbol{M}^{1/2}$ representing the square root of the mobility tensor [59]. Half the blobs along the rod are "passive" with $\tilde{\boldsymbol{u}}_i = 0$, while the other half have an active slip of constant magnitude $|\tilde{\boldsymbol{u}}_i| = u_s$ parallel to the rod's main axis. We can set the active slip at the rear, middle, or front; see Figs. 3(a)–3(c). Here, the background flow is linear shear: $\boldsymbol{u}_0(\mathbf{x}) = \dot{\gamma} z \hat{\mathbf{x}}$.

$$\sum_{i\in(1,N_b)} \boldsymbol{\lambda}_i = \boldsymbol{F}, \qquad \sum_{i\in(1,N_b)} (\boldsymbol{r}_i - \boldsymbol{q}) \times \boldsymbol{\lambda}_i = \boldsymbol{\tau}, \tag{1}$$

$$\sum_{j\in(1,N_b)} \boldsymbol{M}_{ij}\boldsymbol{\lambda}_j = \boldsymbol{u} + \boldsymbol{\omega} \times (\boldsymbol{r}_i - \boldsymbol{q}) - \boldsymbol{u}_0(\boldsymbol{r}_i) + \tilde{\boldsymbol{u}}_i + \sqrt{2k_BT/\Delta t}(\boldsymbol{M}^{1/2}\boldsymbol{W})_i, \quad \text{for } i \in (1, N_b). \tag{2}$$

The linear system (1) and (2) can be interpreted as a regularized discretization of a first-kind boundary-integral equation to solve mobility problems for phoretic particles in viscous flows [55]. After solving Eqs. (1) and (2), we update the configuration with a stochastic integrator [60].

Simulation results.—The placement of the slip region proves to be critical for the configuration of the osmotic flow near the rod. Figures 2(b) and 2(c) show that asymmetrically placed slip results in a contractile (or puller) dipolar flow for front-slip particles, and an extensile (or pusher) dipolar flow for rear-slip particles. The former corresponds to physical long-gold particles, and the latter to short gold particles. Placing the slip region in the middle (symmetric swimmers)—see Fig. 2(a)—yields a higher-

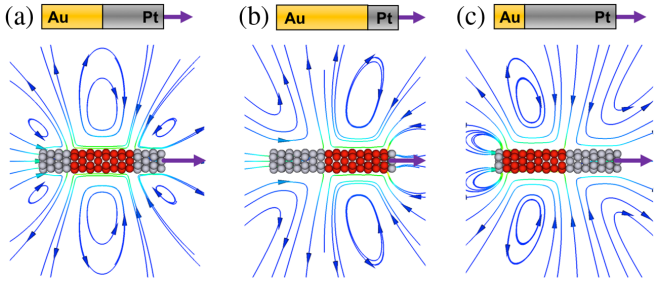

FIG. 2. Computed velocity fields around simulated self-propelled rods with a surface slip region (shown in red) (a) at the center, (b) at the front, and (c) at the rear, corresponding to symmetric, puller, and pusher swimmers, respectively.

order Stokes quadrupole flow as its leading order contribution. This corresponds to a symmetric Au/Pt particle.

In the gap between the rod and the substrate, areas of high (low) pressure appear where surface velocities, both from slip and no-slip regions, converge (diverge); see Figs. 3(a)–3(c). The high pressure node pushes the rod away from the substrate while the low pressure node pulls it down. The tilt angle α mechanically results from the position of the nodes. For a fixed slip coverage, moving the slip–no-slip boundary to the front moves the high pressure region forward and it increases the tilt. Hence, front-actuated rods (i.e., pullers) with larger gold segments assume a larger tilt than symmetric or rear-actuated rods (i.e., pushers); see Fig. 3(d) [51].

The fact of a nonzero tilt angle for ellipsoidal swimmers has been explored most thoroughly by Spagnolie and Lauga [24]; our results provide a mechanical explanation to the equilibrium angle attained by these swimmers. Spherical particles, like squirmers, can show more complex dynamics [61]. For those swimmers the full hydrodynamic traction, and not just the pressure, have to be used to draw conclusions about the preferred orientation.

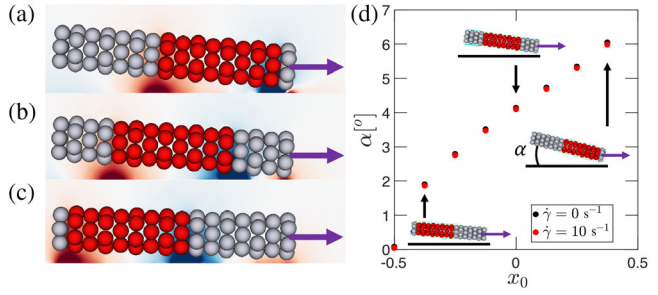

FIG. 3. The tilt angle α is imposed by the position of high (red) and low (blue) pressure nodes in the interstitial space between the rod and the substrate. α decreases as the slip region (red blobs) is moved from front to aft, from puller (a), symmetric (b), to pusher (c). (d) Values of α as a function of the position of the center of the slip layer x_0 (with $x_0 = +0.5, 0, -0.5$ representing front, middle, aft slip) in absence of shear (filled black circles) and a shear $\dot\gamma = 10$ s^{-1} (filled red circles).

The tilt angle α depends weakly on the shear rate but is different for puller, pusher, and symmetric swimmers [see Fig. 3(d)]. It is this tilt that allows the microswimmer to respond to the shear flow near the wall, and is the origin of rheotaxis. We now probe how changes in the tilt angle affect the rods' dynamics in a linear shear flow. We first explore the simulations' predictions to motivate a yet simpler dynamical model of rheotactic response.

Figure 4(a) illustrates the basic rheotactic response evinced by our microswimmer model for all swimmer types (pusher, symmetric, puller). Here, Brownian fluctuations are neglected, and all swimmers are initially set to swim downstream in a linear shear flow. In reaction to the background shear each swimmer turns to swim upstream, with the pusher being the least responsive. For symmetric swimmers, Fig. 4(b) shows the competition between rheotaxis induced by flow with thermal fluctuations whose effect is to decorrelate the swimming direction. In the absence of background flow ($\dot\gamma = 0$ s^{-1}), swimmers diffuse isotropically over long times. This yields a symmetric bimodal distribution $P(V_x)$ for the x velocity V_x. As the shear rate becomes increasingly positive, the distribution becomes asymmetric and increasingly biased towards upstream swimming (negative V_x). The distribution curves also shift right, yielding smaller peak upstream velocities and larger peak downstream velocities.

Weather-vane model.—From these observations we build an intuitive model displaying a behavior akin to that of the weather-vane model proposed by Palacci *et al.* for slightly asymmetric spheres [46]. Because of its downward tilt, the shear flow imposes a larger drag on the tail of a swimming rod. The drag differential promotes upstream orientation by producing a torque that depends on the tilt angle α. The rod's planar position $\boldsymbol{x} = (x, y)$ and orientation angle θ evolve as

$$\dot{\boldsymbol{x}} = V_0 \boldsymbol{n}(\theta) + \dot\gamma h \boldsymbol{e}_x + \sqrt{2D_t}\boldsymbol{W}_x, \tag{3}$$

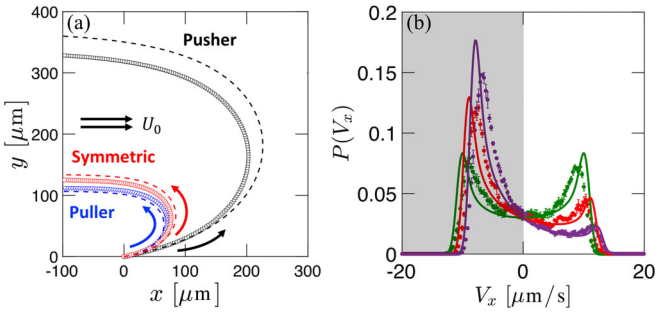

FIG. 4. (a) Trajectories of deterministic swimmers with initial orientation $\theta_0 = \pi/16$, seen from above for simulations (symbols) and theory (dashed lines). (b) Particle velocity distribution in the flow direction (V_x) for hydrodynamic simulations with Brownian noise in a shear flow with $\dot\gamma = 0$ s^{-1} (filled green circles), 4 s^{-1} (filled red circles), and 8 s^{-1} (filled violet circles), and weather-vane model (solid lines).

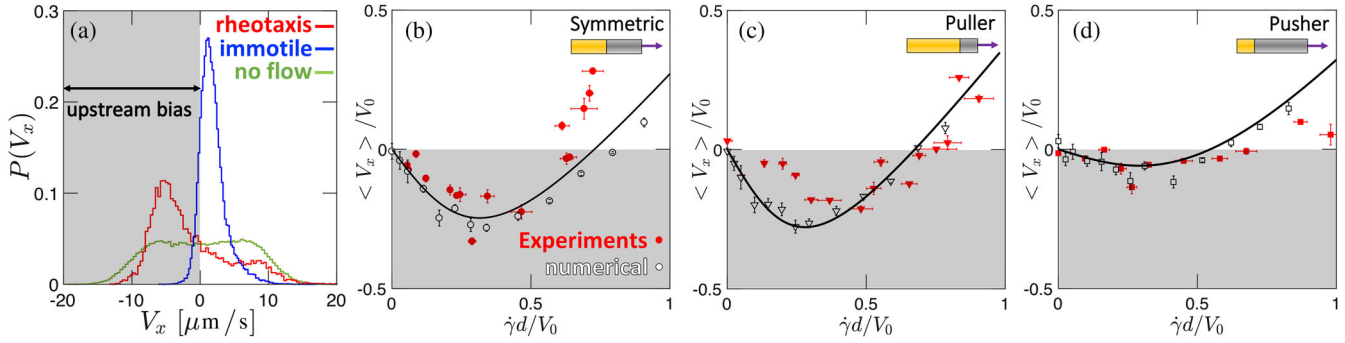

FIG. 5. (a) From experiments: velocity distribution $P(V_x)$ of symmetric swimmers in the absence of background flow (green line), with background flow $\dot{\gamma} = 8.7\ \mathrm{s}^{-1}$ (red line), and for immotile particles in flow $\dot{\gamma} = 9.5\ \mathrm{s}^{-1}$ (blue line). Mean velocity versus shear rates for (b) symmetric, (c) long-gold puller, and (d) short gold pusher swimmers, respectively, in experiments (red symbols) and simulations (open black circles) and compared to the reduced model (black line). Region of upstream swimming bias is shaded in gray.

$$\dot{\theta} = \dot{\gamma} \sin\alpha \sin\theta + \sqrt{2D_r} W_\theta. \tag{4}$$

Equation (3) describes a swimming rod that moves with intrinsic speed V_0 at an angle θ ($\boldsymbol{n} = [\cos(\theta), \sin(\theta)]$), while also advected by a shear flow with speed $\dot{\gamma}h$ at a characteristic height h along the x axis. Equation (4) imposes that the rod angle θ orients against the shear flow. The particle's translational and angular diffusion D_t and D_r are assumed isotropic for simplicity. $\boldsymbol{W}_x$ and W_θ are uncorrelated white noise processes. In the following, all the parameters in Eqs. (3) and (4) are extracted from hydrodynamic simulations at zero shear rate.

This model is sufficient to reproduce the deterministic trajectories of symmetric, puller and pusher swimmers, and agrees with non-Brownian numerical simulations, Fig. 4(a). The tilt angle α controls how fast a rod reorients against the flow and it explains why pushers are less responsive to shear flows. The model also predicts a critical swimming speed to observe positive rheotaxis (upstream swimming). As $\dot{\gamma} \to 0$, the average velocity along the flow is $\langle V_x \rangle = \dot{\gamma}(h - V_0 \sin\alpha / 2D_r)$, which sets the critical speed $V_{0c} = 2D_r h / \sin\alpha$, where the role of the tilt angle is evident.

From Eqs. (3) and (4) we derive the distribution $P(V_x)$ of the swimmer velocities down the channel [51]; see Fig. 4(b). Although the weather-vane model neglects hydrodynamics interactions with the substrate, it agrees with the full numerical simulations for the range of shear rates and also underlines the influence of the critical parameters influencing rheotaxis.

Experimental validation of the theory.—In experiments the velocity distribution $P(V_x)$ follows the same phenomenology described for the numerical simulations and the reduced model; see Fig. 5(a). Under weak shear flow we observe that passive particles (i.e., no H_2O_2) are washed downstream, whereas all three types of active rods orient themselves against the flow and swim upstream.

To compare results from different experiments, where geometrical inhomogeneities in the swimmer population lead to slight variations in the rod propulsions, we scale $\dot{\gamma}$ with the rod's swimming speed V_0 and diameter d. Note that the weather-vane model only predicts positive rheotaxis for shear rates $\dot{\gamma} < V_0/h \approx V_0/d$ even in the deterministic limit ($D_r \to 0$). As suggested by Fig. 4(a), both experiments and simulations reveal that pushers are the least robust rheotactors. Upstream swimming bias is measured by $\langle V_x \rangle$ as a function of the shear rate, shown in Figs. 5(b)–5(d).

Upstream rheotaxis is found for moderate shear rates, $\dot{\gamma}d/V_0 < 0.6$–0.7, with the characteristic nonmonotonic trends previously described [46,47]. The swimmers' ability to move against the flow reaches a maximum at $\dot{\gamma}d/V_0 \sim 0.4$. When the viscous drag overcomes the propulsive forces, i.e., $\dot{\gamma}d/V_0 > 0.7$, the rods enter a drifting regime characterized by a rectilinear downstream motion ($\langle V_x \rangle > 0$). For large shear rates the reduced model predicts a linear average velocity, $\langle V_x \rangle \sim -V_0 + h\dot{\gamma}$. This feature can be used to sort swimmers by their velocity in a microfluidic sieve [49,51,62]. This trend is consistent with numerical and experimental results of Figs. 5(b)–5(d) beyond the minimum of $\langle V_x \rangle$, though with slightly different slopes.

Both the symmetric and asymmetric swimmers' rheotactic behavior agrees with the predictions from simulations and the model. This result corroborates the partial slip model used in the numerical model to describe asymmetric Au/Pt distributions. Qualitatively, simulations indicate that the maximum velocity upstream should be larger for puller and symmetric swimmers than for pushers. Experiments found roughly a factor of 2 difference between the maximum upstream velocities between pushers and pullers at comparable shear values, implying that the reorienting torque is strongest for pullers. This observation further agrees with the deterministic trajectories presented in Fig. 4(a). There, the parameter that differentiates those swimmers' dynamics is their tilt angle α, identifying it as a crucial parameter to engineer efficient rheotactors.

Discussion.—Through experiment, simulation, and modeling, we demonstrate how to modify rheotactic response by changing swimmer type, which for Au/Pt Janus rods amounts to changing the location of the Au/Pt interface. Rheotactic tunability is determined primarily by the tilt angle of the swimmer to the wall, which is controlled by the distribution of the surface slip. The quantitative agreement between experiment and simulation demonstrates that we can infer "by proxy" the pusher and puller nature of artificial microswimmers for which direct flow visualization is often difficult to obtain. Our study extends and elaborates upon the recent results of Ren *et al.* [47] on rheotaxis of symmetric Janus swimmers.

It is chemical reactions that determine the active surface regions. However, our modeling work here, and that of others [24], shows that swimmer-substrate hydrodynamic interactions are sufficient to produce a tilt angle of the rods and thus yield rheotaxis. Our conclusions should apply to other swimmer types besides phoretic particles. A careful treatment of the electrochemical reactions could refine the model of the active slip region used in this work, though solving the electrochemical reactions in the presence of thermal fluctuations is far from trivial [32].

The placement of the slip region opens other routes to design artificial swimmers that have specific interactions with obstacles. For example, particles that swim with their heads up at a wall will tend to move away from it [24]. To explore this idea we numerically designed swimmers that will tilt up [51] by placing an active slip region that covers the nose back to a point forward of the midpoint. This yields a single high pressure node in the front half that tilts up the rod. Placing the slip region on the back half creates a low pressure node on the back half, yielding the same effect. How to experimentally produce Au/Pt swimmers with such slip distributions is an interesting question that we are investigating now.

This work was supported primarily by the MRSEC Program of the National Science Foundation under Award No. DMR-1420073, and also by NSF Grants No. DMS-1463962 and No. DMS-1620331.

[1] D. Saintillan and M. E. Shelley, C.R. Phys. **14**, 497 (2013).
[2] R. E. Goldstein, J. Fluid Mech. **807**, 1 (2016).
[3] C. Bechinger, R. Di Leonardo, H. Löwen, C. Reichhardt, G. Volpe, and G. Volpe, Rev. Mod. Phys. **88**, 045006 (2016).
[4] R. Rusconi and R. Stocker, Curr. Opin. Microbiol. **25**, 1 (2015).
[5] J. Conrad and R. Poling-Skutvik, Annu. Rev. Chem. Biomol. Eng. **9**, 175 (2018).
[6] A. P. Berke, L. Turner, H. C. Berg, and E. Lauga, Phys. Rev. Lett. **101**, 038102 (2008).
[7] S. Elizabeth Hulme, W. R. DiLuzio, S. S. Shevkoplyas, L. Turner, M. Mayer, H. C. Berg, and G. M. Whitesides, Lab Chip **8**, 1888 (2008).
[8] P. Denissenko, V. Kantsler, D. J. Smith, and J. Kirkman-Brown, Proc. Natl. Acad. Sci. U.S.A. **109**, 8007 (2012).
[9] I. D. Vladescu, E. J. Marsden, J. Schwarz-Linek, V. A. Martinez, J. Arlt, A. N. Morozov, D. Marenduzzo, M. E. Cates, and W. C. K. Poon, Phys. Rev. Lett. **113**, 268101 (2014).
[10] E. Lushi, H. Wioland, and R. Goldstein, Proc. Natl. Acad. Sci. U.S.A. **111**, 9733 (2014).
[11] H. Wioland, E. Lushi, and R. Goldstein, New J. Phys. **18**, 075002 (2016).
[12] M. Marcos, H. C. Fu, T. R. Powers, and R. Stocker, Proc. Natl. Acad. Sci. U.S.A. **109**, 4780 (2012).
[13] J. Hill, O. Kalkanci, J. L. McMurry, and H. Koser, Phys. Rev. Lett. **98**, 068101 (2007).
[14] T. Kaya and H. Koser, Biophys. J. **102**, 1514 (2012).
[15] A. Costanzo, R. Di Leonardo, G. Ruocco, and L. Angelani, J. Phys. Condens. Matter **24**, 065101 (2012).
[16] V. Kantsler, J. Dunkel, M. Blayney, and R. E. Goldstein, eLife **111**, e02403 (2014).
[17] N. Figueroa-Morales, G. Leonardo Mino, A. Rivera, R. Caballero, E. Clement, E. Altshuler, and A. Lindner, Soft Matter **11**, 6284 (2015).
[18] E. M. Purcell, Am. J. Phys. **45**, 3 (1977).
[19] K. Drescher, J. Dunkel, L. H. Cisneros, S. Ganguly, and R. E. Goldstein, Proc. Natl. Acad. Sci. U.S.A. **108**, 10940 (2011).
[20] K. Drescher, R. E. Goldstein, N. Michel, M. Polin, and I. Tuval, Phys. Rev. Lett. **105**, 168101 (2010).
[21] C. Dombrowski, L. Cisneros, S. Chatkaew, R. E. Goldstein, and J. O. Kessler, Phys. Rev. Lett. **93**, 098103 (2004).
[22] D. Saintillan and M. J. Shelley, Phys. Rev. Lett. **99**, 058102 (2007).
[23] D. Saintillan and M. J. Shelley, J. R. Soc. Interface **9**, 571 (2012).
[24] S. E. Spagnolie and E. Lauga, J. Fluid Mech. **700**, 105 (2012).
[25] A. Zöttl and H. Stark, Phys. Rev. Lett. **108**, 218104 (2012).
[26] M. Contino, E. Lushi, I. Tuval, V. Kantsler, and M. Polin, Phys. Rev. Lett. **115**, 258102 (2015).
[27] E. Lushi, V. Kantsler, and R. E. Goldstein, Phys. Rev. E **96**, 023102 (2017).
[28] S. Bianchi, F. Saglimbeni, and R. Di Leonardo, Phys. Rev. X **7**, 011010 (2017).
[29] A. Mathijssen, N. Figueroa-Morales, G. Junot, E. Clement, A. Lindner, and A. Zoettl, Nat. Commun. **10**, 3434 (2019).
[30] W. F. Paxton, P. T. Baker, T. R. Kline, Y. Wang, T. E. Mallouk, and A. Sen, J. Am. Chem. Soc. **128**, 14881 (2006).
[31] J. R. Howse, R. A. L. Jones, A. J. Ryan, T. Gough, R. Vafabakhsh, and R. Golestanian, Phys. Rev. Lett. **99**, 048102 (2007).
[32] J. L. Moran and J. D. Posner, J. Fluid Mech. **680**, 31 (2011).
[33] W. Duan, W. Wang, S. Das, V. Yadav, T. E. Mallouk, and A. Sen, Annu. Rev. Anal. Chem. **8**, 311 (2015).
[34] J. L. Moran and J. D. Posner, Annu. Rev. Fluid Mech. **49**, 511 (2017).
[35] D. Takagi, J. Palacci, A. B. Braunschweig, M. J. Shelley, and J. Zhang, Soft Matter **10**, 1784 (2014).
[36] A. T. Brown, I. D. Vladescu, A. Dawson, T. Vissers, J. Schwarz-Linek, J. S. Lintuvuori, and W. C. K. Poon, Soft Matter **12**, 131 (2016).

[37] S. Das, A. Garg, A. I. Campbell, J. Howse, A. Sen, D. Velegol, R. Golestanian, and S. J. Ebbens, Nat. Commun. **6**, 8999 (2015).
[38] C. Liu, C. Zhou, W. Wang, and H. P. Zhang, Phys. Rev. Lett. **117**, 198001 (2016).
[39] J. Simmchen, J. Katuri, W. E. Uspal, M. N. Popescu, M. Tasinkevych, and S. Sánchez, Nat. Commun. **7**, 10598 (2016).
[40] W. E. Uspal, M. N. Popescu, S. Dietrich, and M. Tasinkevych, Phys. Rev. Lett. **117**, 048002 (2016).
[41] M. S. Davies-Wykes, X. Zhong, J. Tong, T. Adachi, Y. Liu, L. Ristroph, M. D. Ward, M. J. Shelley, and J. Zhang, Soft Matter **13**, 4681 (2017).
[42] J. Tong and M. Shelley, SIAM J. Appl. Math. **78**, 2370 (2018).
[43] P. Tierno, R. Golestanian, I. Pagonabarraga, and F. Sagués, Phys. Rev. Lett. **101**, 218304 (2008).
[44] J. Garcia-Torres, C. Calero, F. Sagues, I. Pagonabarra, and P. Tierno, Nat. Commun. **9**, 1663 (2018).
[45] W. Uspal, M. N. Popescu, S. Dietrich, and M. Tasinkevych, Soft Matter **11**, 6613 (2015).
[46] J. Palacci, S. Sacanna, A. Abramian, J. Barral, K. Hanson, A. Y. Grosberg, D. J. Pine, and P. M. Chaikin, Sci. Adv. **1**, e1400214 (2015).
[47] L. Ren, D. Zhou, Z. Mao, P. Xu, T. J. Huang, and T. E. Mallouk, ACS Nano **11**, 10591 (2017).
[48] S. E. Spagnolie, G. R. Moreno-Flores, D. Bartolo, and E. Lauga, Soft Matter **11**, 3396 (2015).
[49] M. Potomkin, A. Kaiser, L. Berlyand, and I. Aranson, New J. Phys. **19**, 115005 (2017).
[50] M. J. Banholzer, L. Qin, J. E. Millstone, K. D. Osberg, and C. A. Mirkin, Nat. Protoc. **4**, 838 (2009).
[51] See Supplemental Material at http://link.aps.org/supplemental/10.1103/PhysRevLett.123.178004 for videos showing the different rheotactic regimes, a description of the numerical method, and further results on the "microfluidic sieve".
[52] D. Qin, Y. Xia, and G. M. Whitesides, Nat. Protoc. **5**, 491 (2010).
[53] A. Goldman, R. Cox, and H. Brenner, Chem. Eng. Sci. **22**, 637 (1967).
[54] S. Delong, F. Balboa Usabiaga, and A. Donev, J. Chem. Phys. **143**, 144107 (2015).
[55] F. Balboa Usabiaga, B. Kallemov, B. Delmotte, A. P. S. Bhalla, B. E. Griffith, and A. Donev, Commun. Appl. Math. Comput. Sci. **11**, 217 (2016).
[56] J. Rotne and S. Prager, J. Chem. Phys. **50**, 4831 (1969).
[57] J. R. Blake, Math. Proc. Cambridge Philos. Soc. **70**, 303 (1971).
[58] J. W. Swan and J. F. Brady, Phys. Fluids **19**, 113306 (2007).
[59] T. Ando, E. Chow, Y. Saad, and J. Skolnick, J. Chem. Phys. **137**, 064106 (2012).
[60] B. Sprinkle, F. Balboa Usabiaga, N. A. Patankar, and A. Donev, J. Chem. Phys. **147**, 244103 (2017).
[61] J. S. Lintuvuori, A. T. Brown, K. Stratford, and D. Marenduzzo, Soft Matter **12**, 7959 (2016).
[62] M. Zaferani, G. D. Palermo, and A. Abbaspourrad, Sci. Adv. **5**, eaav2111 (2019).